1 2 3 4 5 6 7 8 9 10 11 12 13 14 15 16 17 18 19 20 21 22 23 24 25 26 27 28 29 30 31 32 33 34 35 36 37 38 39 40 41 42 43 44 45 46 47 48 49 50 51 52 53 54 55 56 57 58 59 60

Low Temperature Metal Free Growth of Graphene on Insulating Substrates by Plasma Assisted Chemical Vapor Deposition

R. Muñoz,[a] C. Munuera,[a] J. I. Martínez,[a] J. Azpeitia,[a] C. Gómez-Aleixandre[a] and M. García-Hernández[a]

[a.] Instituto de Ciencia de Materiales de Madrid, CSIC
Madrid, 28049, Spain
E-mail: rmunoz@icmm.csic.es; marmar@icmm.csic.es

Direct growth of graphene films on dielectric substrates (quartz and silica) is reported, by means of remote electron cyclotron resonance plasma assisted chemical vapor deposition r-(ECR-CVD) at low temperature (650°C). Using a two step deposition process- nucleation and growth- by changing the partial pressure of the gas precursors at constant temperature, mostly monolayer continuous films, with grain sizes up to 500 nm are grown, exhibiting transmittance larger than 92% and sheet resistance as low as 900 $\Omega\cdot sq^{-1}$. The grain size and nucleation density of the resulting graphene sheets can be controlled varying the deposition time and pressure. In additon, first-principles DFT-based calculations have been carried out in order to rationalize the oxygen reduction in the quartz surface experimentally observed. This method is easily scalable and avoids damaging and expensive transfer steps of graphene films, improving compatibility with current fabrication technologies.

Introduction

Graphene exhibits a number of properties -mechanical stiffness, strength, elasticity, electrical and thermal conductivity- that are superlative [1, 2]. The coexistence of these properties in the same material has placed graphene in the leading position to replace many of the currently used materials in existing applications. For instance, the combination of optical transparency and conductivity, makes it an attractive option as a transparent electrode in photovoltaic solar cells and flexible electronics [3], or the promising applications envisaged for graphene in digital logic and high frequency devices based on its ultrahigh mobility and ambipolar field effect [4], to name two among the possible roles in which graphene reliably could outperform existing technologies [5].

The drawbacks of switching to a new graphene-based technology in industrial processes would be justified if, added to the unique physical properties, the fabrication costs are competitive. The application of graphene in many real world technologies relies on methods to produce large area graphene films without degrading their properties [6,7]. This constraint poses several challenges, which include the development of a harmless transfer process of graphene growth by catalytic CVD or, even better, a transfer-free production technique. Avoiding the post-growth transfer process, besides reducing steps in the production line, is beneficial to ensure graphene properties, since surface/interface contamination, cracks and excessive wrinkles unavoidably form during the transfer, which eventually may lead to lack of continuity or even breakage of the film as the underlying catalyst is removed. In addition, lowering the high growth temperature is also important for practical graphene production.

In this scenario, the game changing breakthrough would be the development of processes to deposit high quality graphene layers on arbitrary substrates, at low temperature. Recently, many approaches have been implemented aiming to overcome this challenge partially or in full [8]. The first approaches involved the direct synthesis on dielectric substrates at elevated temperatures, over 1000°C, in analogy to pyrolytic processes. Atmospheric Pressure CVD (APCVD) synthesis of monolayer or few layer graphene has been realized on Si_3N_4 [9, 10], sapphire (Al_2O_3) [11-13] and SiO_2 [14-16]. Few layer graphene grains have been also deposited on h-BN flakes at 1000°C by APCVD [17] and on MgO nanocrystal powder by low pressure CVD at temperatures between 325°C to 875°C [18]. All these experiments prove the feasibility of metal-catalyst-free growth of graphene on insulating substrates paving the way to transfer-free strategies. However, the high temperatures used limit the compatibility with cost effective fabrication processes. Also on dielectric substrates, the use of Ni [19, 20] or Cu [21] sacrificial films at high synthesis temperatures (over 1000°C) with simultaneous evaporation of catalyst could effectively avoids transfer. However, optimization of the evaporation process would be essential for device fabrication as metal residues remain on the surface, which can be a serious problem for graphene integration into the semiconductor industry.

To address the temperature issue, plasma assisted CVD was proposed as an alternative route to achieve low temperature growth, between 300°C-700°C. The catalytic role of the metallic substrate in decomposing the hydrocarbon precursors is taken over here by the energetic plasma electrons that promote the ionization, excitation and dissociation of the gas carbon source at relatively low temperatures. The first attempts on non-metallic substrates, resulted in graphene with small grain sizes -from 2 to 30 nm- near the limit of amorphous carbon. However, the quality of the films exceeded the graphene oxide counterparts in optoelectronic applications on quartz, SiO_2 and glass [22-24]. Our group already reported the direct and rapid synthesis of nanographene continuous films on cheap commercial glass substrates at temperatures around 500°C by means of a modified r-(ECR-CVD) system using CH_4/Ar gas mixtures [25]. However, there is still much room for improvement in two fundamental aspects: the increase of grain size and the decrease of growth temperature. In general, a low nucleation density and a high growth rate are desired to minimize the grain boundary density that eventually compromises the functional properties of graphene.

Successful enlargement of grain size was achieved with a proposed two-stage growth strategy, to separately control graphene nucleation and edge growth, by high temperature in thermal CVD [10]. Studies on the role of the radicals generated in pure methane plasma [26] showed the competition between the growth effects of CxHy radicals and the etching effect of atomic H at low temperature, proving that the intensity of the etching effect of atomic H is temperature dependent and is a crucial factor on the nucleation, growth rate, and growth model. This temperature dependence of the hydrogen etching effect was used to switch between the nucleation and the edge growth stages, by using pure methane plasma [27]. Based on this two-step route and with the careful tuning of the different parameters, grain sizes close to 500nm and, in isolated cases, growth temperatures below 600°C were achieved. However, the accurate control over the number of layers remained elusive and the low reported mobility for the continuous films posed a major hurdle for applications in optoelectronics.

In order to enhance the electrical properties of the as-grown graphene on dielectric substrates, Wei et al. went a step beyond, taking advantage of the hydrogen etching ability by

1
2
3
4
5
6
7
8
9
10
11
12
13
14
15
16
17
18
19
20
21
22
23
24
25
26
27
28
29
30
31
32
33
34
35
36
37
38
39
40
41
42
43
44
45
46
47
48
49
50
51
52
53
54
55
56
57
58
59
60

introducing a extra H_2 pressure during growth [28]. Promising results were obtained in SiO_2 substrates, in terms of size of isolated grains and growth temperature but a high temperature annealing (1000°C) of the substrates prior to growth was required. In addition, high mobility values were measured on single grains, but no results were reported on continuous films making it difficult, the direct comparison with Cu-CVD grown graphene. Nonetheless, the reported values for the electrical (~4 $k\Omega \cdot sq^{-1}$) and optical properties (97.6% at 550 nm) for continuous graphene films grown on transparent sapphire substrate endorse this strategy as a promising growth method for future graphene electronics [28].

Still, compared to the enumerated advances achieved in the catalyst-free growth of graphene on some dielectric substrates (e. g. SiO_2, Si_3N_4, Al_2O_3, $SrTiO_3$ or h-BN), the direct growth on the ordinary transparent insulating solid glasses has been achieved with limited success. Either the temperatures needed are still high (1000°C) [29], or small grain sizes and high values of sheet resistance are reported for low-temperature growth [22].

In this work we have dealt with the improvement of the direct growth of graphene films on transparent solid glasses (quartz, fused silica). We have addressed the direct growth at low temperature, the enlargement of the grain size by controlling the nucleation density and, not so often addressed, the control over the number of layers. Following the two-stage growth strategy and using a C_2H_2/H_2 gas mixture, we succeeded in both, lowering the growth temperature (T < 700°C) and increasing the grain size, by using r-(ECR-CVD). The improvements in grain size and quality observed at submonolayer coverage lead to better functional properties of the continuous film, with markedly low sheet resistance value (>900 $\Omega \cdot sq^{-1}$) and transmittance over 92%, thus combining the complementary intrinsic properties of graphene and glasses. Furthermore, the protocol developed is easily scalable and avoids damaging and expensive transfer processes of graphene films, improving compatibility with current fabrication technologies.

Experimental Section

Synthesis

Plasma assisted r-(ECR-CVD) technique has been used as it provides higher efficiency at low power in the dissociation of gas species than other plasma sources, and allows deposition on large areas [30]. The system consists of an ASTEX AX 2000 microwave power source, a two zone chamber and a two stage pumping system (see ref. 25 for further details on the experimental set-up). Amorphous fused silica and quartz were used as substrates. The two-step process is aimed at separately controlling graphene nucleation and growth stages. In the first stage, it is essential to nucleate high quality graphitic seeds, monolayer thick and with controlled coverage. In the second stage, the goal is to promote the edge-growth of the already nucleated grains, preventing further nucleation or the etching of previous deposited material. To achieve these targets, the various parameters (time (t), temperature (T) and partial pressures (PC_2H_2 and PH_2)) have been controllably tuned at the nucleation (t_1, T_1, $P_1C_2H_2/P_1H_2$) and growth (t_2, T_2, $P_2C_2H_2/P_2H_2$) stages. A post-growth low temperature annealing was applied in UHV, improving the final properties of the film.

1 2 3 4 5 6 7 8 9 10 11 12 13 14 15 16 17 18 19 20 21 22 23 24 25 26 27 28 29 30 31 32 33 34 35 36 37 38 39 40 41 42 43 44 45 46 47 48 49 50 51 52 53 54 55 56 57 58 59 60

Characterization

Raman spectroscopy has been carried out by a confocal Raman microscope (Witec alpha-300R). Raman mapping and spectroscopy were obtained using a 532nm excitation laser and a 100x objective lens (NA = 0.9). The incident laser power was 1mW. Atomic force microscopy (AFM) measurements were performed with a commercial head and software from Nanotec [31] operated at room temperature. Two different operation modes have been employed: dynamic mode, exciting the tip at its resonance frequency (~75 kHz), to simultaneously acquire topographic and phase images, and contact mode to acquire simultaneous topographic and lateral force images. X-ray photoelectron spectra (XPS) were recorded using an instrument from Specs equipped with a PHOIBOS 150 MCD analyzer and Al Kα X-ray source (1486.6 eV) operating at 12.5 kV and 250 W. The chamber base pressure is 3×10^{-10} mbar. The acquisitions were performed at a pass energy of 40 eV (energy resolution 1.0 eV). Full and core-level XPS spectra were acquired on bare quartz substrate and graphene on quartz sample, after annealing at 150°C. The intensities were estimated by calculating the integral of each peak after the subtraction of adequate background lines with the help of CasaXPS and UNIFIT-2009 softwares; atomic ratios were then derived using the theoretically calculated cross-sections given in the NIST Reference Databases [32]. The performance of the continuous films was characterized by means of UV-Vis-NIR spectrophotometry (SHIMADZU SolidSpec– 3700 Spectrophotometer) for transmittance and four point probe measurement (JANDEL RMS2 Universal Probe) with continuous current (from 1 µA -100 µA) for sheet resistance.

Theoretical Methods

In the *ab initio* atomistic simulations, total energies, forces, and stresses were minimized (for both structure and lattice) by using DFT as implemented in the accurate plane-waves package QUANTUM ESPRESSO[33]. A perturbative van der Waals (vdW) correction was used to check for the effect of long-range interactions on the different configurations analysed [34,35]. A generalized gradient approximation (GGA) parametrization[36] has been used for the exchange and correlation potential, and norm-conserving scalar-relativistic pseudopotentials have been used to model the ion−electron interaction[37]. Activation energies and transition states (TSs) have been investigated within the climbing-image nudge elastic band (CI−NEB) approach [38] implemented in the QUANTUM ESPRESSO package,[33] where the initial, the final, and all the intermediate image-states were free to fully relax. Quartz [11-20] surface was modelled in a repeated slab geometry: *i)* a slab of five physical quartz layers (H-passivated at its bottom part) with a minimum distance of ~ 25 Å of vacuum between neighbouring cells along the axis perpendicular to the surface; as well as *ii)* full periodic boundary conditions representing an infinite surface with perfectly balanced stoichiometry in order to avoid polarization effects. In all the relaxation processes the two bottom layers were kept fixed during the relaxation to account the bulk effect. All the Brillouin zones (BZ) were sampled by means of optimal Monkhorst-Pack grids [39], guaranteeing a full convergence in energy and electronic density. We repeated some of the calculations by including an extra physical quartz layer finding no significant variations in total energy.

1 2 3 4 5 6 7 8 9 10 11 12 13 14 15 16 17 18 19 20 21 22 23 24 25 26 27 28 29 30 31 32 33 34 35 36 37 38 39 40 41 42 43 44 45 46 47 48 49 50 51 52 53 54 55 56 57 58 59 60

Results and discussion

Step 1: Deposition of graphitic nuclei

The main objective here is to nucleate monolayer-thick, high quality graphitic seeds, and control their density. To these purposes we explored systematically the parameter space on silica substrates. The effect of the H_2 included in the gas mixture on the structure of the deposit, was initially determined at different temperatures. The role of atomic hydrogen as an etchant for avoiding amorphous carbon and graphene deposition has been previously exploited [26]. Appropriate H content in the atmosphere, appears to be a necessary but not a sufficient condition to grow a carbonaceous crystalline material. Indeed, low temperature ECR-CVD for diamond deposition resulted eventually in microcrystalline graphitic deposit [40]. To select an optimum nucleation temperature, we took into account recent studies of atomic H interaction with graphene, that indicated maximum etching around 450°C, decreasing at higher temperature [41], with lower etching efficiency in the basal plane and on few layer graphene than in the edges and monolayer graphene [42]. Regarding the precursor, C_2H_2, dehydrogenation reaction starting from 400°C and cracking of carbon bond over 600°C [43] was reported on silicon based surfaces. Overall, these reactions are essential as the mobility of resulting species varies. It is also important to take into account that graphitization was reported starting from 400°C [43, 44]. Taking these data into account, experiments were performed in the range of 550°C, selected as a compromise between low temperature deposition, surface diffusion and efficient graphitization, and 700°C, chosen over carbon bond cracking, at the limit of H etching. Figure 1 collects the main results of these experiments by directly comparing Raman spectra and AFM measurements of the samples grown at both temperatures, for t_1=60min. At T_1= 550°C, P_1H_2 was varied in the range (0 : 35 sccm), keeping constant a small amount of carbon precursor, $P_1C_2H_2$ (0.25 sccm). For the growth at hight temperature, T_1= 700°C, the variation range of P_1H_2 is also increased (35:55 sccm), since the etching efficiency decreases with temperature. Figure 1a shows the Raman spectra of the samples at T_1= 550°C, for different P_1H_2 values. As P_1H_2 increases, the crystallinity of the nuclei increases, as confirmed by the D, G peaks narrowing and the emerging 2D peak. However, the simultaneous appearance of D´, D+G bands indicate that some deviation from pure graphitic network was introduced into the lattice. Presumably, the small size of the nuclei, as well as atomic H could still have influence at this temperature on this issue [45]. Hydrogenation could result in the formation of C-H sp3 bonds as well as the breaking of the translational symmetry of C=C sp2 bonds. The morphological characterization of this sample by AFM is shown in figure 1b, for P_1H_2 = 35sccm. Isolated clusters, with mean diameter ~50nm and height ~1.5-2nm, are formed after 60min of growth. Figure 1 (c, d) presents the Raman and AFM results of the experiments performed at 700°C to directly compare with the growth at 550°C. Higher P_1H_2 is needed to avoid amorphous deposits due to less activity of H with T. Raman spectra of the samples show that, as P_1H_2 increases, the crystallinity of the nuclei increases as well, confirmed by the D, G narrowing. The 2D peak remains nearly unchanged. For the highest P_1H_2 explored (55 sccm), the height of the 2D is similar to the height of the G peak. This is indicative of the decrease of nuclei thickness. However the D peak intensity in relation to G peak is higher than at T= 550°C. Presumably, smaller grain size of the nuclei play a role, even though we can not rule out that some hydrogen remains. The higher coverage obtained at 700°C hinders the

direct measure of layer thickness. Nonetheless, as shown in figure S1, we can use the AFM tip to sweep the continuous film and estimate the number of layers. From these thickness measurements, it is evident that thinner films are grown when higher temperatures are used.

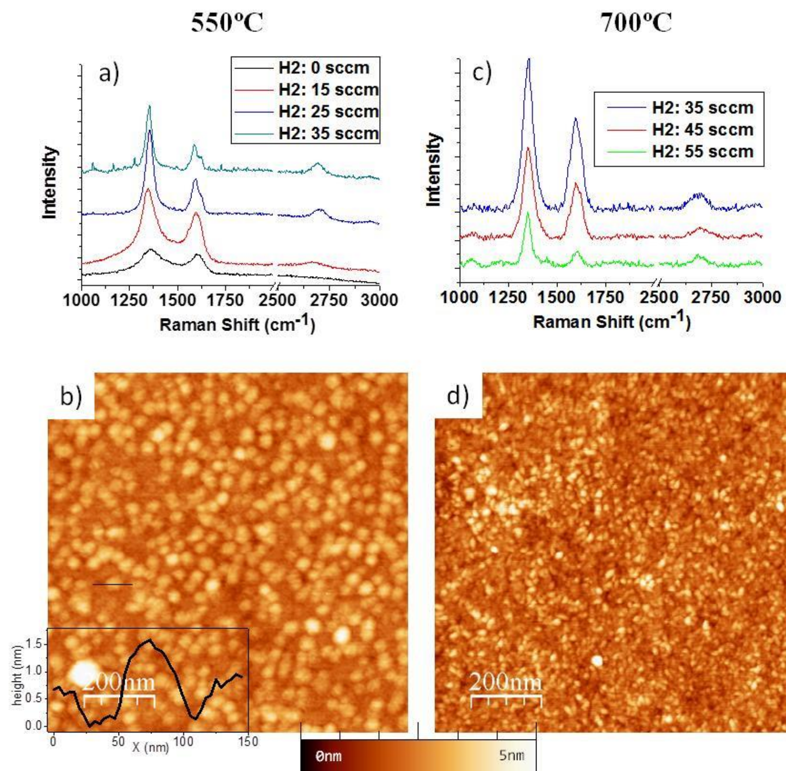

Figure 1. **Nuclei deposition at T=550°C for t1= 60 min**. a) Raman spectra at varying P_1H_2. First experiment at H_2=0 included Ar to sustain the plasma. $Ar/H_2/C_2H_2$= 35/0/0.25 (sccm). Subsequent experiments: H_2/C_2H_2= 15:35/0.25 (sccm). $PC_2H_2 = 1.2\times10^{-4}$ mbar, PT = $1.6\text{-}3.4\times10^{-2}$ mbar, Power = 100 W. b) AFM topographic image of the deposit at H2= 35 sccm. **Nuclei deposition at T=700 °C for t1= 60 min**. c) Raman spectra at P_1H_2: H_2/C_2H_2 = 35: 55/0.25 (sccm); $PC_2H_2 = 1.2\times10^{-4}$ mbar; P_T = 3.4- 5.4×10^{-2} mbar; Power = 100 W. d) AFM topographic image of the deposit at H_2= 55 sccm.

From these sets of experiments we conclude that a proper H atmosphere avoids nucleation of amorphous material from carbon radicals CxHy. Also, at higher temperature, the H activity decreases and therefore, the amount of H has to be increased. This is in agreement to what it has been observed on graphene films of monolayer or multilayer nature exposed to hydrogen rich plasma, aforementioned [41, 42]. We observe that at T=700°C the thickness of the nuclei is decreased down to monolayer or bilayer graphene. A plausible explanation is that the substrate morphology induces graphene lattice distortions resulting in enhanced reactivity, more evident in monolayer than few layer films, since monolayer corrugation is higher. In our low temperature experiments, this effect is coupled with the high H activity that avoids nucleation of monolayer graphene in favorable points and, instead, stabilizes tridimensional structures as nanocrystalline graphite or bilayer graphene [27]. However, at higher temperature around 700°C, the H activity on the emerging monolayer nuclei is negligible, restricted to boundaries. Hence, monolayer deposit can be stabilized in favorable points. The lateral size of the grains is also smaller for the higher temperature. This is related to carbon bond breaking as

1 2 3 4 5 6 7 8 9 10 11 12 13 14 15 16 17 18 19 20 21 22 23 24 25 26 27 28 29 30 31 32 33 34 35 36 37 38 39 40 41 42 43 44 45 46 47 48 49 50 51 52 53 54 55 56 57 58 59 60

well as to a limited mobility of the resulting precursors. Carbon bond breaking might occur on silica surface over 600°C [43]. The resulting monomers have higher sticking coefficient than dimmer hydrocarbons and their mobility is lower.

Step2: Increase the grain size

In the previous step, best results were attained at T_1=700°C and P_1H_2= 55sccm and, consequently, they were taken as the optimal nucleation parameters. Still, prior to focusing on the edge growth of these nuclei, we optimized the nucleation density, to obtain coverages much lower than those shown in figure 1. This is accomplished by reducing t_1, the nucleation time. To assess this relation, a set of growth varying t_1 has been performed and, the resulting nuclei density, characterized by AFM. Directly measuring isolated tiny graphitic clusters deposited at 700°C on the relatively rough glass substrates is a difficult task. To facilitate this characterization, the initial nuclei have been enlarged, modifying the parameters in the second stage of the growth process, to favor edge growth over nucleation. In this growth stage, the partial pressure PC_2H_2 (instead of PH_2, because of its negligible influence on the total pressure) is decreased to enlarge the domains from their edges during a time (t_2). These enlarged grains are easier identified by AFM, facilitating the study of nucleation density versus t_1. As shown in the supplementary information, figure S2, by reducing t_1 to 30min and subsequently switching to edge growth for t_2=120min, significant decrease in nuclei density and increase in grain size is obtained when compared with figure 1, in both fused silica and quartz substrates. But this figure also highlights that deposition on silica rendered important inhomogeneities in the nucleation process, probably related to a random increase of the roughness during the H_2 etching. For this reason, after confirming that the nucleation protocol devised for silica holds also in quartz, we refer from now onwards to the results obtained in quartz substrates to facilitate the fine tuning of the nucleation and growth parameters.

Figure 2 shows the results, on quartz, of the influence of t_1 on nucleation density, by keeping t_2 constant, equal to 300 minutes. PC_2H_2 was decreased from 0.25sccm to 0.20sccm to switch from nucleation to growth stage. The images show that these growth parameters provide submonolayer coverage where size distribution and nucleation density can be studied by AFM. The data presented in figure 2 confirms that the nucleation density increases with t_1 from 5min to 10min, following a linear relationship. The grain size distribution is very similar for both t_1 values with average equivalent diameters of 100-120nm (figure 2c), as expected for an equal edge growth time (t_2). Comparing figure 1 and 2 it is evident that by changing the partial pressure (PH_2/PC_2H_2) we can switch between nucleation and edge growth. However, images and histograms in figure 2 show that the final grains are not uniform in size, with diameters ranging from 50nm to 200nm. This is consistent with secondary nucleation taking place in this second step of the growth process, if favorable nucleation points, in terms of local surface energy, are not fully saturated during the nucleation stage. Edge growth can even be resumed after sample has been taken out of the growth chamber. After ex-situ characterization, the sample of figure 2(b) was introduced again in the chamber for additional edge growth. Prior to further growth, the sample is exposed to moderate etching by H_2 at 500°C during 5 min to remove functionalization due to air exposition. Figure S3 shows the increase in grain size for further growth (180 min) for the sample with t_1= 10 min, proving the

capability of the method to control nucleation and growth stages by tuning the partial pressures.

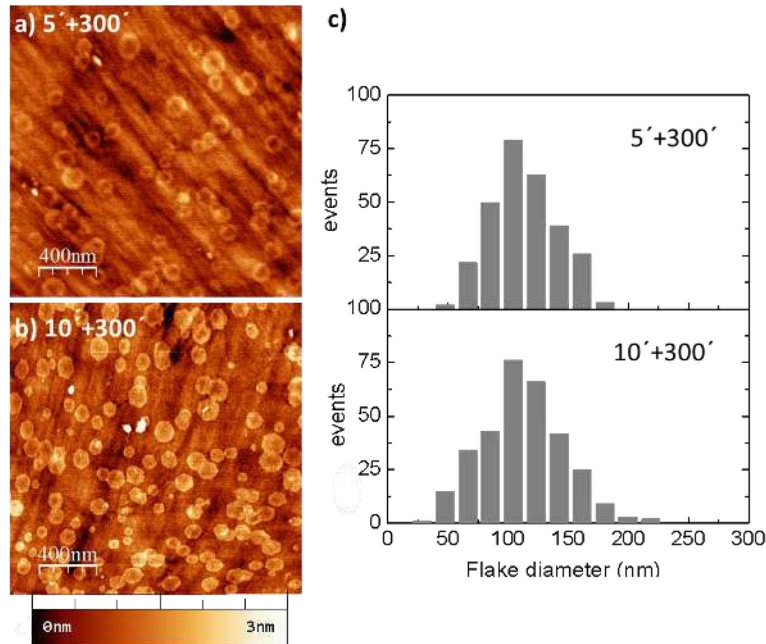

Figure 2. **Graphene on quartz at T = 700°C**. H_2 / C_2H_2 = 55/0.25:0.20 (sccm), P_T = 5.4×10^{-2} mbar: P = 100 W. a, b) AFM topographic images of graphene deposition for increasing nucleation time t_1= 5min and 10min, and equal growth time, t_2 =300 min. The density of graphene flakes, calculated from 10 different images, is 14 flakes/µm^2 and 30 flakes/µm^2, respectively. c) Histograms showing the equivalent graphene flake diameter distribution for equal t_2.

Once addressed the ability to switch between nucleation and edge growth by modifying the partial pressure, and analyzed the effect of t_1 and t_2 on the corresponding stage, best results were achieved for t_1=5 min and t_2= 9 h, as shown in Fig. S4. These samples exhibited graphene crystals with sizes around 400 nm and perfect hexagonal shape suggesting their single crystal nature. Secondary signal channels in AFM have proven very useful in revealing information sometimes difficult to detect, or even hidden, in topographic images. This is evident in figure S4b, where graphene flakes are straightforward identified in simultaneously acquired phase images, even if they are hardly visible in topography. Even more revealing is the lateral force image (figure S4(d)) acquired when measuring in contact mode, where it can be clearly seen that the graphene flakes present an internal structure resembling few layer graphene in many points. There are not systematic studies on the tuning of the number of layers of the graphenic depositions on insulating substrates. One possible reason could be the difficulty in determining the number of layers for individual graphene grains grown on dielectric substrates: grain sizes are still in the resolution limit for accurate determination of the number of layers using Raman analysis, and height measurements with AFM is hindered normally by the rough substrates, that present height differences of the order (or even higher than) the layer thickness. We demonstrate below that, by using lateral force images to reveal internal features within the flakes, such as step edges between layers, investigation on the control over the number of layers can be tackled.

In order to inquire into the density of bilayer and few layer inclusions, the AFM tip was used to sweep away the graphene flakes by increasing the applied force in contact mode. Figure S5 shows simultaneous topographic and lateral force images before (fig. S5(a) and (b)) and after (fig. S5 (e) and (f)) removing some graphene flakes. Line profiles measured along the flakes (fig. 5S (c) and (d)) reveal that, once removed, etch pits 1.5-2nm deep are observed in the substrate, at the position of the flakes, indicating some sort of erosion during growth process. To prevent the likely influence of the erosion on the formation of multilayer flakes, due to the local increase of the substrate roughness, the growth temperature was slightly decreased. Figure 3 shows the two temperature limits explored (from 650°C to 700°C). Intermediate stages are included in the supporting information (figure S6). Lateral force images show that at T=700°C, flakes with more than five layers are predominant (Figure 3(a)). In most cases, as revealed by the images, similar interlayer orientation is found, particularly for the bottom layers, suggesting a Bernal stacking. Twisted stacking is also found on some grains and, in some cases, the formation of clusters with no recognizable geometrical pattern (top left corner of figure 3a). The parallel hexagonal layers resemble the inverted wedding cake (IWC) structures already published in catalytic growth [46]. Slightly decreasing the temperature (650°C) leads to the growth of predominantly single layer graphene grains with diameters reaching the half micron, randomly oriented over the surface (figure 3b). The perfect hexagonal shape of most graphene crystals deposited suggests their single crystal nature. High magnification lateral force images measured within single grains (figure 3c) reveal the atomic lattice periodicity of graphene, with lattice orientation parallel to the edges of the grain.

The quality of the samples was further evaluated by using Raman mapping and spectroscopy. The mapping signals were extracted from the integrated intensities of the characteristic graphene Raman peaks, G (∼1595 cm^{-1}) and 2D (∼ 2704 cm^{-1}). Particularly interesting for the comparison of samples is the ratio of 2D intensity to that of the G band (I_{2D}/I_G), plotted in figure 3d-e. This ratio, along with the full width at half-maximum (FWHM) of the 2D peak is often used to determine the graphene layer numbers. For both samples, Raman I_{2D}/I_G mapping shows inhomogeneous signal over micron scale, with bright patches corresponding to the graphene flakes. But, since plotted with the same color scale, it is clear that absolute values differs considerably between samples, with average $I_{2D}/I_G< 1$ for the sample grown at 700°C and $I_{2D}/I_G> 3$ for the 650°C. Since the grain size is close to the resolution limit of the confocal Raman, the hexagonal shape clearly visible in AFM images is not resolved in Raman mapping. Still, the grain size is large enough to allow positioning the spot within individual grains and recording the corresponding spectra. Several individual spectra acquired at grain positions, for both samples, are depicted in figure 3f-g, where the difference in I_{2D}/I_G ratio is evident. The 2D peak possesses a symmetric shape with a single Lorentzian profile, yielding best full width at half-maximum (FWHM) of 40 cm^{-1} and 30 cm^{-1} for the samples grown at 700°C and 650°C, respectively. Thus, Raman analysis strongly indicates the formation of predominantly monolayer graphene on the sample grown at 650°C, in agreement with the AFM measurements. The high I_{2D}/I_G ratio and the low $2D_{FWHM}$ obtained for this sample confirm the high quality of the grown graphene, among the best obtained from direct growth on dielectric substrates. The D peak, associated to defects, is also observed in the spectra, and mainly due to the presence of edges or strain. At this respect, the exact position of the G and 2D peaks was assessed, resulting in mean values of G ∼1596 cm^{-1}, 2D ∼ 2710 cm^{-1} for the

sample grown at 700°C and G ~1599 cm^{-1}, 2D ~ 2706 cm^{-1} for the sample grown at 650°C. These values points to a compressive strain effect induced in the graphene flakes when grown on quartz, similar to that reported for other dielectric substrates [47].

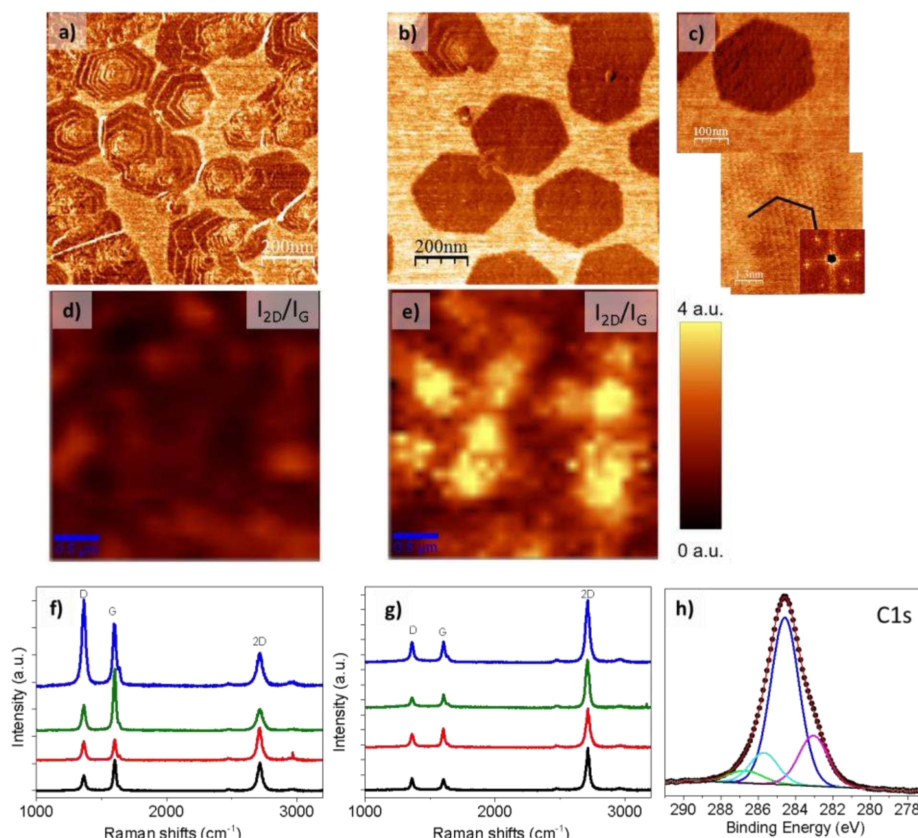

Figure 3. Graphene on quartz at H_2 / C_2H_2 = 55/0.25:0.20 (sccm), P_T = 5.4×10^{-2} mbar: P = 100 W for 5 min nucleation time, 9 hour growth. AFM lateral force image of the sample grown at a) T= 700°C and b) T= 650°C (corresponding topographic images are included in figure S6). c) High magnification lateral force image of a single flake from sample grown at 650°C. Image below shows the atomic lattice periodicity corresponding to the flake in c). The inset is the Fast-Fourier transform of the periodicity image. d, e) Raman mapping of the 2D/G intensity ratio (I_{2D}/I_G) for the samples grown at 700°C and 650°C, respectively. f, g) Individual spectra acquired at grain positions, for both samples. h) High resolution XPS C1s core level spectrum (black dots) of the sample grown at 650°C. The spectrum was fitted with four peaks: blue (284.6 eV), green (286.5 eV), cyan (285.6 eV) and magenta (283 eV). See main text for the assignment of the corresponding peaks. Color scale: a) 4mV; b) 10mV; c) 7mV

High-resolution X-ray photoelectron spectroscopy (XPS) measurements were performed on the sample grown at 650°C in order to assess the interface between graphene and quartz substrate. The characteristic XPS C 1s core-level spectrum (Figure 3h) was fitted with four peaks, corresponding to the different chemical environment of the carbon atoms. The dominant peak is the C-sp^2 component (284.6 eV) that confirms the graphitic structure of the grains. The peaks located at higher binding energy are assigned to C-H (285.6 eV), likely originating from H-terminated edges, and C-O (286.5 eV) species. At lower binding energy (283 eV) there is a component whose origin can be ascribed to remainders of the growth process (e.g. C_2H_4Si at 282.5 eV) or to the interaction of the deposited carbon with the quartz substrate (e.g. SiC C(1s) is 282.5-283.5 eV). However, as shown in Figure S7, the formation of SiC (100.6 eV) can be ruled out from the corresponding Si2p spectra. Therefore, if present, the interaction might be with low-coordination Si atoms at the surface, without the nucleation of

SiC compound. Additional XPS spectra are presented in Figure S7, both for graphene sample and quartz substrate, measured in the same conditions for proper comparison. The full XPS spectra confirms the absence of signals from metals such as Fe, Co, Ni, and Cu, as expected from the direct growth on the dielectric substrate. Interestingly, the comparison of graphene sample and substrate spectra (fig. S7(a)) clearly confirms that, even in this high quality sample, there is a decrease in the oxygen content during synthesis (see quantitative values in fig. S7). This is indicative of the substrate reduction upon graphene growth, with is supported also by the broadening and the slight shift towards lower binding energy of the Si2p for the grown sample. Still, C1s and Si2p core-level spectra discard the formation of SiC during graphene growth.

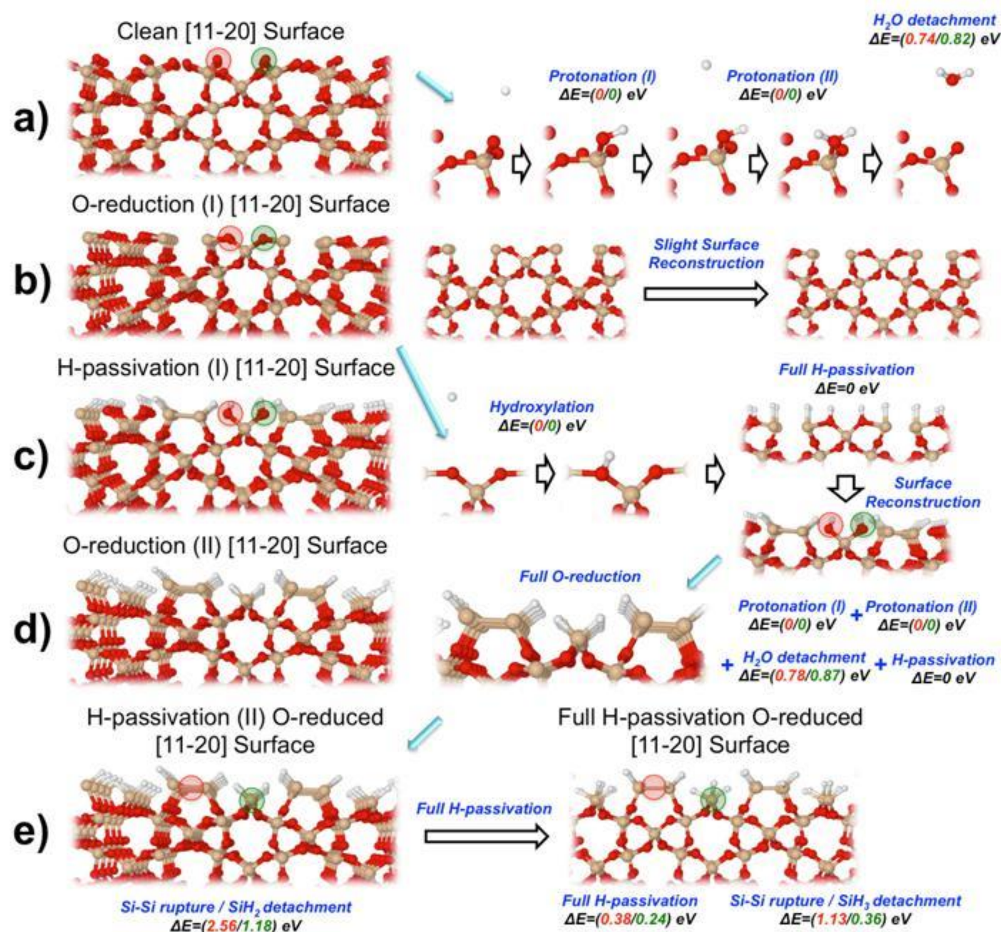

Figure 4. **O-reduction of the [11-20] quartz surface.** (a) Side view of the clean hydroxylated [11-20] quartz surface containing four hydroxyl ions per unit cell, in which the top two-coordinated surface silicon atoms are involved in hydroxylation and two dangling oxygen atoms in protonation. This surface possesses both germinal and vicinal hydroxyl groups. This surface configuration resulting from our calculations matches very well with the findings from previous literature[48]. In panel (a) we also show the two subsequent protonation barrierless steps on each dangling oxygen atom towards the final detachment of two H_2O molecules per unit cell. (b) Once the water molecules are detached the surface suffers a slight reconstruction. (c) Hydroxylation of the hydroxyl ions induces the rupture of Si—O bonds towards the formation of new Si—Si bonds, which, after full H-passivation of the surface, leaves two OH terminating groups. (d) These OH terminating groups are reduced again by subsequent barrierless protonation steps, leading to the detachment of H_2O molecules. At this stage of the O-reduction we have a Si-rich surface partially H-passivated. (e) The activation barriers to break the Si—Si bond (2.56 eV) and to detach a SiH_2 (1.18 eV) are shown in the figure. Nevertheless, at very low activation energies (0.24—0.38 eV) each Si atom on the surface still permits the accommodation of another H atom. At this stage the activation barriers to break the Si—Si bond and to detach a SiH_3 are reduced to 1.13 and 0.36 eV, respectively.

1 2 3 4 5 6 7 8 9 10 11 12 13 14 15 16 17 18 19 20 21 22 23 24 25 26 27 28 29 30 31 32 33 34 35 36 37 38 39 40 41 42 43 44 45 46 47 48 49 50 51 52 53 54 55 56 57 58 59 60

The reduction process of the quartz surface was simulated and is supported with theoretical calculations. We modeled the (11-20) face (X-cut) of our quartz samples assessing the activation energies for the probable reaction paths (Fig. 4). Protonation of surface oxygen with atomic hydrogen from plasma and subsequent water vapor release are highly probable in this surface at synthesis temperature. The passivation of the silicon enriched surface with hydrogen prior growth is also favored because the silicon detachment is more energy demanding.

Continuous films

The ultimate goal of the catalyst-free growth of graphene is to deposit continuous films with suitable properties. Therefore, once growth parameters were explored at submonolayer coverage, the study of continuous films is addressed. We first examined the self-limiting character of the deposition procedure with continuous layer. Figure 5 presents an AFM morphological characterization after complete coverage. The continuity of this film was confirmed by four point probe measurements with a sheet resistance around 3.4 $k\Omega \cdot sq^{-1}$. Figures 5 (a-b) depict the surface morphology, where two trends of domain merging are highlighted: hexagonal graphene domains of presumably similar orientation often generate a smooth lateral merging that result in seamless interfaces between grains, presenting domain boundaries without linear defects (Fig. 5(b), black arrows). In this way, generated domains could coalesce resulting in a single crystal layer even with high nucleation density [49-54]. On the other hand, the images clearly show that a rough lateral merging also takes place at many points, where linear defects occur (Fig. 5(b), pink line).

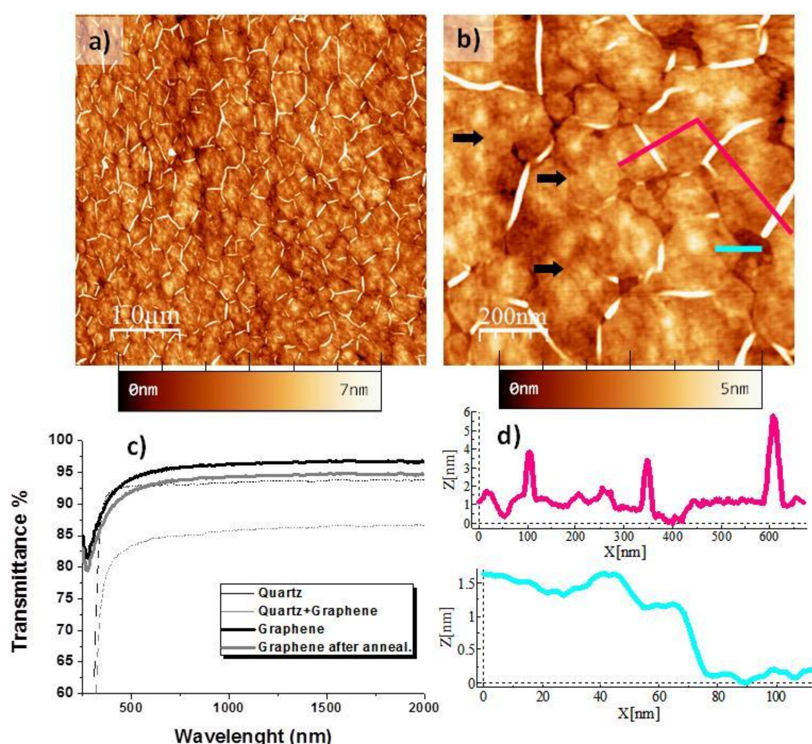

Figure 5. **Characterization of continuous film** T = 650 °C, H_2/C_2H_2 = 55/0.25:0.20 (sccm), $P_T = 5.4 \times 10^{-2}$ mbar: P = 100 W. a-b) AFM topographic images of graphene deposition on quartz for 5 min nucleation time and 10 hour growth. Black arrows in b) highlight smooth lateral merging of graphene grains. c) Transmittance spectra before (95%) and after (92%) post-growth annealing. d) Height profiles taken along the corresponding lines in b) showing the height of the linear defects formed upon grain coalescence (pink) and the film thickness (cyan).

On these defects carbon species accumulate. This final behavior might be similar than the observed in vertical graphene deposition [55]. The coalescence and the local accumulation of the carbon material in those linear defects, indicates that the process is not completely self-limiting, even though leaving pristine basal plane in terms of carbon addition. From transmittance characterization, measured by UV-Vis-NIR spectrophotometry (fig. 5(c)), it is also clear that there is an influence of this accumulation on the transmittance of the film, which yields values over 95%, lower than in typical monolayer graphene.

Post-growth annealing

Given the synthesis protocol described, the presence of adsorbed hydrogen at the grain boundaries is highly likely. To assess the influence of this hydrogen on the functional properties of the continuous films, a mass-sensitive thermal desorption experiment was performed in a vacuum system (base pressure 4.9×10^{-10}mbar) equipped with a quadrupole mass spectrometer. After growth, the sample was annealed in vacuum, increasing the temperature stepwise up to 600°C (below the synthesis temperature). Figure S8(a) shows the measured spectra of the partial pressures of the desorbing molecules, acquired with the mass spectrometer, which senses the mass to charge ratio (m/z) of the molecule. Among the typical surface adsorbed species due to ambient air (H_2O, CO, CO_2) high amount of hydrogen H-H_2 was captured. In figure S8(b)-(c) a comparison of the sample morphology prior and after annealing is presented. The overall aspect has not changed upon annealing, but small holes (below 1nm deep) are observed preferentially forming between grains. The height and density of the linear defects is also lower after the annealing process. The most notable difference after thermal desorption is the impressive change in the sheet resistance value, that decreased from around 3.4 $k\Omega\cdot sq^{-1}$ to 900 $\Omega\cdot sq^{-1}$. Further experiments should be carried out to assess this point, but we postulate that, after deposition, hydrogen remains in the grain boundaries driving the formation of sp3 structure that suffer some kind of conversion to sp2 after annealing, in a similar way of hydrogen desorption from graphane already published [56]. The resulting quality factor after annealing exceeds the quality of typical graphene oxide and liquid phase exfoliation graphene electrodes [57].

Conclusions

We have explored the role and the critical behavior of hydrogen and temperature in the graphene synthesis by plasma assisted chemical vapor deposition r-(ECR_CVD), confirming that, by fine tuning the different parameters, highly crystalline monolayer graphene can be deposited in dielectric surfaces. Using a two-step deposition process- nucleation and growth- mostly monolayer films, with grain sizes up to 500 nm are synthesized on silica and quartz at 650°C. Data on the nucleation density, edge growth and thickness control is provided with the study of samples with submonolayer coverages. The combination of different spectroscopic and microscopic techniques proves the high quality of the synthesized graphene and also discloses an oxygen reduction process undergone by the quartz substrate upon graphene growth. This reduction process has been simulated by DFT-based calculations.

1
2
3
4
5
6
7
8
9
10
11
12
13
14
15
16
17
18
19
20
21
22
23
24
25
26
27
28
29
30
31
32
33
34
35
36
37
38
39
40
41
42
43
44
45
46
47
48
49
50
51
52
53
54
55
56
57
58
59
60

Functional properties are measured on continuous samples, exhibiting transmittance over 95% and sheet resistance ~3.4k$\Omega \cdot sq^{-1}$. Mass-spectrometer analysis reveals a significant release of hydrogen upon post-growth annealing in UHV, presumably from the grain boundaries, adsorbed during synthesis. An improvement in the sheet resistance value (900 $\Omega \cdot sq^{-1}$) is achieved after the thermal process, with a small decrease of the transmittance (92%), related to the conversion from sp3 to sp2 after hydrogen desorption.

The avoidance of a transfer step, the high reliability of the process as well as the compatibility of this method with current applied technologies make this approach a promising route for scalable graphene deposition on dielectrics.

Acknowledgements

We acknowledge funding by the EC under the Graphene Flagship Pilot and the Graphene Flagship (grant agreement no. 604391). JA acknowledges funding from FPI Program of MINECO (BES-2012-058600). JIM acknowledges funding from the ERC-Synergy Program (Grant ERC-2013-SYG-610256 NANOCOSMOS) and computing resources from CTI-CSIC. CM acknowledges the financial support by the “Ramón y Cajal” Program of MINECO (RYC-2014-16626). The “Servicio de Espectroscopia de Fotoelectrones (XPS/ESCA)” at CITIUS is kindly acknowledged for the XPS measurements.

References

[1] Geim A K, Novoselov K S 2007 The rise of graphene *Nat. Mater*. ***6*** 183.

[2] Castro Neto A H, Guinea F, Peres N M R, Novoselov K S, Geim A K 2009 The electronic properties of graphene *Rev. Mod. Phys*. **81** 109.

[3] Bae S *et al* 2010 Roll-to-roll production of 30-inch graphene films for transparent electrodes *Nat. Nanotech*. **5** 574.

[4] Schwierz F 2010 Graphene transistors *Nat. Nanotechnol.* **5** 487.

[5] Ferrari A C *et al* 2015 Science and technology roadmap for graphene, related two-dimensional crystals, and hybrid systems *Nanoscale* **7** 4598.

[6] Novoselov, K. S.; Geim, A. K.; Morozov, S. V.; Jiang, D.; Zhang, Y.; Dubonos, S. V.; Grigorieva, I. V.; Firsov, A. A. *Science.* **2004***, 306*, 666.

[7] Morozov S V, Novoselov K S, Katsnelson M I, Schedin F, Elias D C, Jaszczak J A, Geim A K 2008 Giant Intrinsic Carrier Mobilities in Graphene and Its Bilayer *Phys. Rev. Lett.* **100** 016602.

[8] Chen X, Wua B, Liu Y 2016 Direct preparation of high quality graphene on dielectric substrates *Chem. Soc. Rev*. **45**, 2057.

[9] Sun J, Lindvall N, Cole M T, Teo K B K, Yurgens A 2011 Large-area uniform graphene-like thin films grown by chemical vapor deposition directly on silicon nitride *Appl. Phys. Lett.* **98** 252107.

[10] Chen J, Guo Y, Wen Y, Huang L, Xue Y, Geng D, Wu B, Luo B, Yu G, Liu Y 2013 Two-Stage Metal-Catalyst-Free Growth of High-Quality Polycrystalline Graphene Films on Silicon Nitride Substrates *Adv. Mater.* **25** 992.

[11] Hwang J *et al* 2013 van der Waals Epitaxial Growth of Graphene on Sapphire by Chemical Vapor Deposition without a Metal Catalyst *ACS Nano* **7** 385.

[12] Song H J, Son M, Park C, Lim H, Levendorf M P, Tsen A W, Park J, Choi H C 2012 Large scale metal-free synthesis of graphene on sapphire and transfer-free device fabrication *Nanoscale* **4** 3050.

[13] Jerng S K, Yu D S, Kim Y S, Ryou J, Hong S, Kim C, Yoon S, Efetov D K, Kim P, Chun S H 2011 Nanocrystalline Graphite Growth on Sapphire by Carbon Molecular Beam Epitaxy *J. Phys. Chem. C.* **115** 4491.

[14] Sun J, Lindvall N, Cole M T, Wang T, Booth T J, Boggild P, Teo K B K, Liu J, Yurgens A 2012 Controllable chemical vapor deposition of large area uniform nanocrystalline graphene directly on silicon dioxide *J. Appl. Phys.* **111** 044103.

[15] Chen J, Wen Y, Guo Y, Wu, B, Huang L, Xue Y, Geng D, Wang D, Yu G, Liu Y 2011 Oxygen-Aided Synthesis of Polycrystalline Graphene on Silicon Dioxide Substrates *J. Am. Chem. Soc.* **133** 17548.

[16] Chen J et al. 2014 Near-Equilibrium Chemical Vapor Deposition of High-Quality Single-Crystal Graphene Directly on Various Dielectric Substrates *Adv. Mater*. **26** 1348.

[17] Ding X, Ding G, Xie X, Huang F, Jiang M 2011 Direct growth of few layer graphene on hexagonal boron nitride by chemical vapor deposition *Carbon* **49** 2522.

[18] Rümmeli M H, Bachmatiuk A, Scott A, Börrnert F, Warner J H, Hoffman V, Lin J, Cuniberti G, Büchner B 2010 Direct Low-Temperature Nanographene CVD Synthesis over a Dielectric Insulator *ACS Nano.* **4** 4206.

[19] Xiong W, Zhou Y S, Jiang L J, Sarkar A, Mahjouri-Samani M, Xie Z Q, Gao Y, Ianno N J, Jiang L, Lu Y F 2013 Single-Step Formation of Graphene on Dielectric Surfaces*Adv. Mater.* **25** 630.

[20] Yan Z, Peng Z, Sun Z, Yao J, Zhu Y, Liu Z, Ajayan P M, Tour J M 2011 Growth of Bilayer Graphene on Insulating Substrates *ACS Nano* **5** 8187.

[21] Ismach A, Druzgalski C, Penwell S, Schwartzberg A, Zheng M, Javey A, Bokor J, Zhang Y 2010 Direct Chemical Vapor Deposition of Graphene on Dielectric Surfaces *Nano Lett.* **10** 1542.

[22] Malesevic A, Vitchev R, Schouteden K, Volodin A, Zhang L, Van Tendeloo G, Vanhulsel A, Van Haesendonck C 2008 Synthesis of few-layer graphene via microwave plasma-enhanced chemical vapour deposition *Nanotechnology* **19** 305604.

[23] Zhang L, Shi Z, Wang Y, Yang R, Shi D, Zhang G 2011 Catalyst-free growth of nanographene films on various substrates *Nano Res.* **4** 315.

[24] Medina H, Lin Y-C, Jin C, Lu C-C, Yeh C-H, Huang K-P, Suenaga K, Robertson J, Chiu P-W 2012 Metal-Free Growth of Nanographene on Silicon Oxides for Transparent Conducting Applications *Adv. Funct. Mater.* **22** 2123.

[25] Muñoz R, Gómez-Aleixandre C 2014 Fast and non-catalytic growth of transparent and conductive graphene-like carbon films on glass at low temperature J. Phys. D: Appl. Phys. **47**, 045305.

[26] Zhang L, Ni M, Liu D, Shi D, Zhang G 2012 Competitive Growth and Etching of Epitaxial Graphene *J. Phys. Chem. C* **116** 26929

[27] Liu D, Yang W, Zhang L, Zhang J, Meng J, Yang R, Zhang G, Shi D 2014 Two-step growth of graphene with separate controlling nucleation and edge growth directly on SiO_2 *Carbon* **72** 387.

[28] Wei D, Lu Y, Han C, Niu T, Chen W, Wee A T S 2013 Critical Crystal Growth of Graphene on Dielectric Substrates at Low Temperature for Electronic Devices *Angew. Chem. Int. Ed*. ***52*** 14121.

1 2 3 4 5 6 7 8 9 10 11 12 13 14 15 16 17 18 19 20 21 22 23 24 25 26 27 28 29 30 31 32 33 34 35 36 37 38 39 40 41 42 43 44 45 46 47 48 49 50 51 52 53 54 55 56 57 58 59 60

[29] Sun J *et al* 2015 Direct Chemical Vapor Deposition-Derived Graphene Glasses Targeting Wide Ranged Applications Nano Lett. **15** 5846.

[30] Yoon S F, Tan K H, Rusli J, Ahn , Huang Q F 2000 Effect of microwave power on diamond-like carbon films deposited using electron cyclotron resonance chemical vapor deposition *Diamond Relat. Mater*. **9** 2024.

[31] Horcas I, Fernández R, Gómez-Rodríguez J M, Colchero J, Gómez-Herrero J, Baro A M 2007 WSXM: A software for scanning probe microscopy and a tool for nanotechnology *Rev. Sci. Instrum*. **78** 013705.

[32] NIST X-ray photoelectron spectroscopy database: http://srdata.nist.gov/xps/.

[33] Giannozzi P *et al* 2009 QUANTUM ESPRESSO: a modular and open-source software project for quantum simulations of materials. J. Phys. Condens. Matter. **21** 395502.

[34] Barone V, Casarin M, Forrer D, Pavone M, Sambi M, Vittadini A 2009 Role and Effective Treatment of Dispersive Forces in Materials: Polyethylene and Graphite Crystals as Test *Cases J. Comput. Chem.* **30** 934.

[35] Grimme S 2006 Semiempirical GGA-type Density Functional Constructed with a Long-range Dispersion Correction *J. Comp. Chem*. **27** 1787.

[36] Zhang Y, Yang W 1998 Comment on "Generalized Gradient Approximation Made Simple" *Phys. Rev. Lett*. **80** 890.

[37] Vanderbilt D 1990 Soft Self-consistent Pseudopotentials in a Generalized Eigenvalue Formalism. *Phys. Rev. B* **41** 7892.

[38] Berne B J, Cicotti G, Coker D 1998 Classical and Quantum Dynamics in Condensed Phase Simulations Eds.; World Scientific Publishing Company: Singapore.

[39] Monkhorst H J, Pack J D 1976 Special Points for Brillouin-zone Integrations *Phys. Rev. B* **13** 5188.

[40] Eddy C R Jr., Sartwell B D, Youchison D L 1991 Diamond thin film growth on silicon at temperatures between 500 and 600°C using an electron cyclotron resonance microwave plasma Source *Surf. Coat. Technol*. **48** 69.

[41] Yang R, Zhang L, Wang Y, Shi Z, Shi D, Gao H, Wang E, Zhang G 2010 An Anisotropic Etching Effect in the Graphene Basal Plane *Adv. Mater*. **22** 4014.

[42] Diankov G, Neumann M, Goldhaber-Gordon D 2013 Extreme Monolayer-Selectivity of Hydrogen-Plasma Reactions with Graphene *ACS Nano*. **7** 1324.

[43] Nishijima M, Yoshinobu J, Tsuda H, Onchi M 1987 The adsorption and thermal decomposition of acetylene on Si(100) and vicinal Si(100) 9° Surf. Sci. **192** 383.

[44] Cullis C F, Franklin N H 1964 The Pyrolysis of Acetylene at Temperatures from 500 to 1000°C. *Proc. R. Soc. London, Ser. A: Mathematical and Physical Sciences* **280** 139.

[45] Luo Z, Yu T, Kim K-J, Ni Z, You Y, Lim S, Shen Z, Wang S, Lin J 2009 Thickness-Dependent Reversible Hydrogenation of Graphene Layers *ACS Nano* **3** 1781.

[46] Li Q, Chou H, Zhong J-H, Liu J-Y, Dolocan A, Zhang J, Zhou Y, Ruoff R S, Chen S, Cai W 2013 Growth of Adlayer Graphene on Cu Studied by Carbon Isotope Labeling *Nano Lett*. **13** 486.

[47] Sun J *et al*. 2014 Direct Growth of High-Quality Graphene on High-κ Dielectric $SrTiO_3$ Substrates *J. Am. Chem. Soc.* **136** 6574.

[48] Koretsky C M, Sverjensky D A, Sahai N 1998 Calculating site densities of oxides and silicates from crystal structures *Am. J. Sci*. **298** 349.

[49] Lee J-H *et al* 2014 Wafer-scale growth of single-crystal monolayer graphene on reusable hydrogen-terminated germanium *Science* **344** 286.

[50] Strupinski W *et al* 2011 Graphene Epitaxy by Chemical Vapor Deposition on SiC *Nano Lett*. **11** 1786.

[51] Nguyen V L, Lee Y H 2015 Towards Wafer-Scale Monocrystalline Graphene Growth and Characterization *Small* **11** 3512.

[52] Yang W *et al* 2013 Epitaxial growth of single-domain graphene on hexagonal boron nitride *Nat. Mater*. **12** 792.

[53] Tang S *et al* 2013 Precisely aligned graphene grown on hexagonal boron nitride by catalyst free chemical vapor deposition *Sci. Reports.* **3** 2666.

[54] Zhang L, Shi Z, Liu D, Yang R, Shi D, Zhang G 2012 Vapour-phase graphene epitaxy at low temperatures *Nano. Res*. **5** 258.

[55] Bo Z, Yang Y, Chen J, Yu K, Yan J, Cen K 2013 Plasma-enhanced chemical vapor deposition synthesis of vertically oriented graphene nanosheets *Nanoscale* **5** 5180.

[56] Elias D C 2009 Control of graphene's properties by reversible hydrogenation: evidence for graphane *Science* **323** 610.

[57] De S, Coleman J N 2010 Are there fundamental limitations on the sheet resistance and transmittance of thin graphene films? *ACS Nano* **4** 2713.

View publication stats